













RESEARCH ARTICLE | DECEMBER 09 2024

Magnetic field-induced topological phase transition for colossal negative magnetoresistance in EuB_6

Lulu Pan ; Yunhao Wang ; Xiang Ding ; Guojing Hu; Hui Guo; Senhao Lv; Guoyu Xian; Qi Qi; Ke Zhu; Yechao Han; Minyinan Lei; Zhuolin Li ; Lihong Bao ; Ying Zhang ; Xiao Lin; Shiyu Zhu  ; Rui Peng ; Haitao Yang  ; Hong-Jun Gao 

 Check for updates

Appl. Phys. Lett. 125, 243101 (2024)

<https://doi.org/10.1063/5.0236038>



View Online



Export Citation

Articles You May Be Interested In

Berry curvature induced antisymmetric in-plane magneto-transport in magnetic Weyl EuB_6

Appl. Phys. Lett. (October 2022)

Magnetic topological Kondo semimetal phases of matter

Appl. Phys. Lett. (August 2024)

Enhanced colossal electroresistance in $\text{Cu/Pr}_{0.7}\text{Ca}_{0.3}\text{MnO}_3/\text{Cu}$ structure

J. Appl. Phys. (November 2006)



Applied Physics Letters

Special Topics Open for Submissions

[Learn More](#)

Magnetic field-induced topological phase transition for colossal negative magnetoresistance in EuB_6

Cite as: Appl. Phys. Lett. **125**, 243101 (2024); doi: [10.1063/5.0236038](https://doi.org/10.1063/5.0236038)

Submitted: 30 August 2024 · Accepted: 24 November 2024 ·

Published Online: 9 December 2024



View Online



Export Citation



CrossMark

Lulu Pan,¹ Yunhao Wang,¹ Xiang Ding,² Guojing Hu,¹ Hui Guo,^{1,3} Senhao Lv,^{1,4} Guoyu Xian,^{1,5} Qi Qi,^{1,3} Ke Zhu,^{1,3} Yechao Han,³ Minyinan Lei,² Zhuolin Li,^{1,3} Lihong Bao,^{1,3,5} Ying Zhang,^{1,3} Xiao Lin,³ Shiyu Zhu,^{1,3,a)} Rui Peng,² Haitao Yang,^{1,3,5,a)} and Hong-Jun Gao^{1,3,5}

AFFILIATIONS

¹Beijing National Center for Condensed Matter Physics and Institute of Physics, Chinese Academy of Sciences, Beijing 100190, People's Republic of China

²Advanced Materials Laboratory, State Key Laboratory of Surface Physics and Department of Physics, Fudan University, Shanghai 200433, People's Republic of China

³School of Physical Sciences, University of Chinese Academy of Sciences, Beijing 100049, People's Republic of China

⁴Division of Functional Material Research, Central Iron and Steel Research Institute, Beijing 100081, People's Republic of China

⁵Songshan Lake Materials Laboratory, Dongguan, Guangdong 523808, People's Republic of China

^{a)}Authors to whom correspondence should be addressed: syzhu@iphy.ac.cn and htyang@iphy.ac.cn

ABSTRACT

EuB_6 , as a magnetic Weyl semimetal, has attracted much attention in recent years due to its rich intriguing physical properties, especially the colossal negative magnetoresistance (CNMR) exceeding -80% and the topological phase transition. Yet, the underlying mechanism of the CNMR in EuB_6 is still controversial. In this work, the CNMR with a maximum value of -88.4% and Hall resistivity without linear dependence on the magnetic field are both observed to indicate the existence of a weak ferromagnetic order below 50 K. The effective carrier concentration can be modulated by both temperatures and external magnetic fields. Moreover, the angle-resolved photoelectron spectroscopy results demonstrate the gradual band splitting and crossing near the Fermi level below 15 K, and the field-dependent Kelvin probe force microscope results confirm the field-induced variation of the Fermi level at different temperatures. Furthermore, by integrating those results with the monotonic increment relationship between the effective carrier concentration and the field-induced magnetization ratio, it is concluded that the magnetic field-induced topological phase transition is the main mechanism for the CNMR in EuB_6 , which is helpful to understand the exotic transport properties in magnetic topological materials. Our findings provide a route for exploring and manipulating the topology-related transport properties via the external magnetic field in other systems with strong correlation between magnetism and topological states.

Published under an exclusive license by AIP Publishing. <https://doi.org/10.1063/5.0236038>

Topological materials have attracted extensive attention due to their exotic transport properties and potential application in future quantum devices.^{1–3} The initial milestone is the discovery of the quantum Hall effect (QHE). Therein, the Hall resistance is quantized while the longitudinal resistance of the sample boundary is zero under a high external magnetic field.^{4,5} It is highly desirable to control the excellent transport behavior by modulating the topological state through intrinsic band structure adjustments or external fields. An attempt has been made to realize the quantum anomalous Hall (QAH) effect by introducing ferromagnetic properties into the topological

insulator.^{6,7} In recent years, the tremendous progress has been achieved in some systems where magnetism and topology intertwine,⁸ for instance, the ferromagnetic Weyl semimetal $\text{Co}_3\text{Sn}_2\text{S}_2$ (Ref. 9) and the antiferromagnetic topological insulator MnBi_2Te_4 .¹⁰ Moreover, the topological states can be modulated by strain, light, and electrical and magnetic fields in some unique systems such as ZrTe_5 ,^{11,12} CsV_3Sb_5 ,¹³ MnBi_2Te_4 ,¹⁴ Na_3Bi ,¹⁵ and Fe-doped $(\text{Bi,Sb})_2\text{Se}_3$ heterostructures.¹⁶ Consequently, the interaction between magnetism and topology becomes one of the significant topics in the condensed state matter physics. From the perspective of a fundamental investigation, an

intrinsic magnetic topological material with a simple crystal structure and clear electronic band structure might be an excellent system to clarify the correlation mechanism.

EuB_6 possesses a simple cubic crystal structure and is a magnetic topological Weyl semimetal at low temperatures. The topological band structure near the Fermi level is simple and clear without any other interference. Moreover, it is predicted to realize the large-Chern-number quantum anomalous Hall effect (QAHE) in its [111]-oriented quantum-well structures according to the theoretical calculation.¹⁷ Thus, EuB_6 is an ideal platform to reveal the exotic transport properties, especially to investigate the correlation between magnetism and topology. In experimental studies, the typical magneto-transport property of EuB_6 is the colossal negative magnetoresistance (CNMR).¹⁸ Yet the mechanism of that CNMR remains contentious, with two main explanations including the electronic phase separation¹⁹ and the magnetic fluctuations.²⁰ Nonetheless, the influence of the magnetic field on the topological band structure is not well considered, and the contribution of the topology in EuB_6 to the CNMR is unclear.

In this paper, the transport properties, magnetic properties, angle-resolved photoelectron spectroscopy (ARPES), and Kelvin probe force microscope (KPFM) measurements are carried out on the high-quality EuB_6 single crystal. The paramagnetic (PM)–ferromagnetic (FM) phase transition is observed with the temperature decreasing. The CNMR and the Hall resistivity without linear dependence on the magnetic field are observed within the same temperature range. The ARPES measurement results demonstrate the gradual band splitting and crossing near the Fermi level with the temperature decreasing.²¹ Moreover, the field-induced variation of the Fermi level is observed at different temperatures by the KPFM measurement. Based on the above-mentioned results and the monotonic increment relationship between the effective carrier concentration and the field-induced magnetization ratio, it can be concluded that the CNMR of EuB_6 predominantly originates from the magnetic field-induced topological phase transition.

The EuB_6 single crystal is prepared by an Al-flux method,²² and the corresponding structure characterizations confirm the high quality of the as-grown EuB_6 single crystals (see details in Fig. S1). Based on the high-quality single crystal, the magnetoresistance (MR) curves are measured at different temperatures [Fig. 1(a)]. Overall, the MR curves decrease first and then increase with the external field increasing. The external field corresponding to the maximum negative MR ratio is defined as the critical magnetic field ($B_c@MR$, where $\delta MR = 0$). As shown in Fig. 1(b), the temperature and the critical magnetic field have almost the same influence on the maximum negative MR ratio and the CNMR ratio exceeding -88% is achieved around 12 K. MR curves ranging from -1.5 to $+1.5$ T [the inset of Fig. 1(b)] do not show the distinctive sharp cusps corresponding to the weak localization (WL) effect.²³ Therefore, the WL effect can be excluded. The upwarp of the temperature-dependent longitudinal resistivity ($\rho_{xx} \sim T$) curves in the inset of Fig. 1(c) indicate the possible Kondo effect.^{24,25} However, it could only contribute a small negative MR ratio of $\sim -8\%$ (estimated in Fig. S2), which is far from the main mechanism for the CNMR in EuB_6 .

The dramatic decrease in the temperature-dependent ρ_{xx} under the zero field below 15 K [Fig. 1(c)] suggests a possible phase transition at the critical temperature of 15 K. The monotonic shift of the maximum values of $d\rho_{xx}/dT$ with the external field increasing [Fig. S3(b)]

indicates that the phase transition could be related to the magnetic ordered states. In order to determine the magnetic ordered states, the temperature-dependent magnetization ($M \sim T$) curves under the corresponding external fields are measured [Fig. 1(d)]. The $M \sim T$ curve in the inset demonstrates a PM–FM phase transition with a critical temperature of 15 K (Ref. 26) (detailed in Fig. S4), which is the same as the critical temperature in the $\rho_{xx} \sim T$ curve measured under 0 T. Moreover, the $M \sim T$ curves under different external fields show a similar shifting behavior compared to the $\rho_{xx} \sim T$ curves in Fig. 1(c). So far, it can be supposed that the transport properties, including the CNMR, are closely related to not only the temperature-dependent magnetization but also the field-induced magnetization in EuB_6 . Numerically, such huge CNMR ratio of $\sim -88\%$ is impossible to happen only by the suppression of the scattering between carriers and the magnetic moments after applying the external field.²⁴ Fundamentally, the carrier concentration mainly determines the electronic resistivity, which can be investigated by the Hall resistivity.

The temperature-dependent Hall resistivity ($\rho_{xy} \sim T$) curves are measured under different external fields [Fig. 2(a)]. The upward shift of the $\rho_{xy} \sim T$ curves with the external field increasing suggests the ordinary Hall-type behavior. It should be noted that the measured ρ_{xy} is primarily contributed by the ordinary Hall effect since the AHE signal is rather tiny ($< 5 \mu\Omega \text{ cm}$) as discussed in Fig. S5. The decrease in ρ_{xy} with the decreasing of the temperature in Fig. 2(a) reflects the increase in the effective carrier concentration ($N_{\text{eff}} = B/(e\rho_{xy})$,²⁷ where e is the elementary charge) in EuB_6 . As shown in Fig. 2(b), $\rho_{xx} \sim T$ curves, as well as $d\rho_{xx}/dT \sim T$ curves, measured under $B = 0.05$ and 0 T almost overlap, which shows that the transport behavior under 0.05 T can be used to proximately reflect the intrinsic transport parameters under 0 T. The temperature-dependent N_{eff} curve under 0.05 T shows a critical temperature of 15 K, similar to the value in the $\rho_{xx} \sim T$ curve measured under 0 T. In addition, N_{eff} increases with the decrease in the temperature and the increase in the external field [Fig. 2(c)]. To further investigate the influence of the external field on N_{eff} , the field-dependent ρ_{xy} and N_{eff} curves are shown in Figs. 2(d) and 2(e). The ρ_{xy} , without linear dependence on the external field is observed from 4 to 35 K, and the nonlinear dependence is enhanced with the temperature increasing [Fig. 2(d)]. N_{eff} initially increases and then slightly decreases with the external field increasing [Fig. 2(e)], reaching its maximum value under the critical external field ($B_c@N_{\text{eff}}$), where $\delta N_{\text{eff}} = 0$ at different temperatures from 4 to 35 K. The temperature-dependent $B_c@MR$ and $B_c@N_{\text{eff}}$ exhibit the similar variation tendencies and approximate values at the same temperatures [Fig. 2(f)]. Therefore, the maximum N_{eff} corresponds to the maximum negative MR, which indicates the field-induced variation of N_{eff} should be responsible for the CNMR in EuB_6 . In addition, the field-dependent N_{eff} means that the carrier pocket, as well as the electronic band structures near the Fermi level, could be effectively changed by the external magnetic field, which is analogous to the reported temperature-induced variation of the band structures in EuB_6 .^{21,28}

In the current temperature-induced topological phase transition in EuB_6 observed via the ARPES experiments, discrepancies arise in both the Fermi level locations and the transition temperatures.^{21,28,29} To validate the influence of the temperature on the band structures, the temperature-dependent ARPES measurements were carried out from 30 to 6.9 K. The measured band structures along M–X remains unchanged from 30 to 17 K [Figs. 3(b–I)–3(b–III)] at which the EuB_6

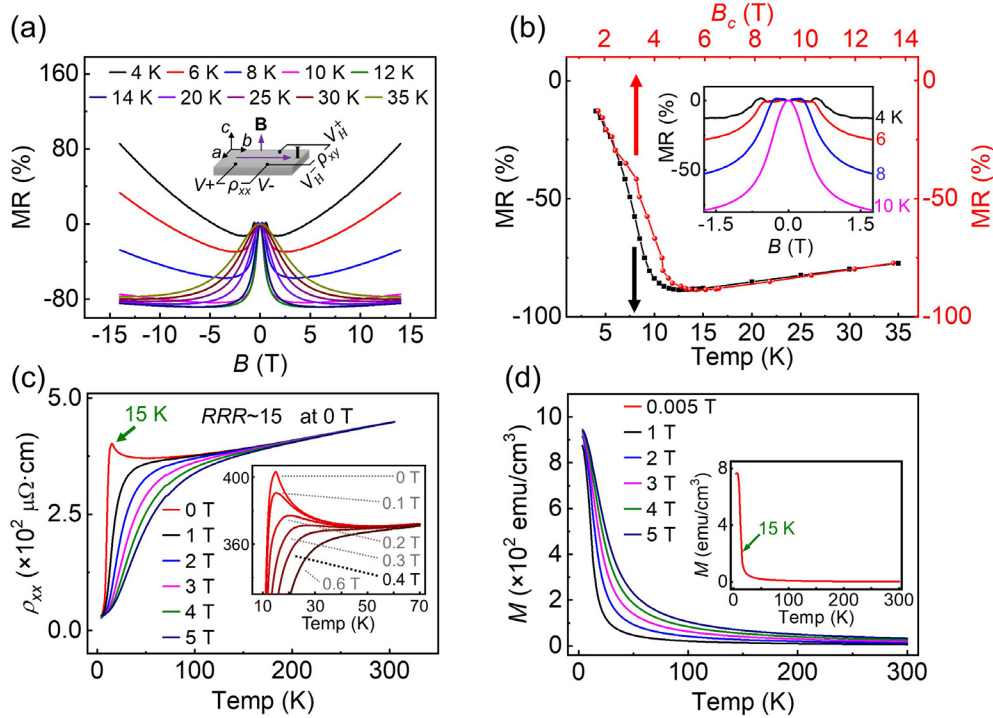


FIG. 1. (a) MR ratio curves at different temperatures. The inset illustrates the measurement configuration. (b) The maximum negative MR ratio as a function of the temperature and the corresponding critical external magnetic field ($B_c@MR$). The inset shows the MR curves at the small external field (± 1.5 T) from 4 to 10 K. (c) $\rho_{xx} \sim T$ curves under different external fields. The inset shows the corresponding curves with external fields from 0 to 0.6 T. (d) $M \sim T$ curves under different external fields. The inset shows the $M \sim T$ curve measured under 0.005 T.

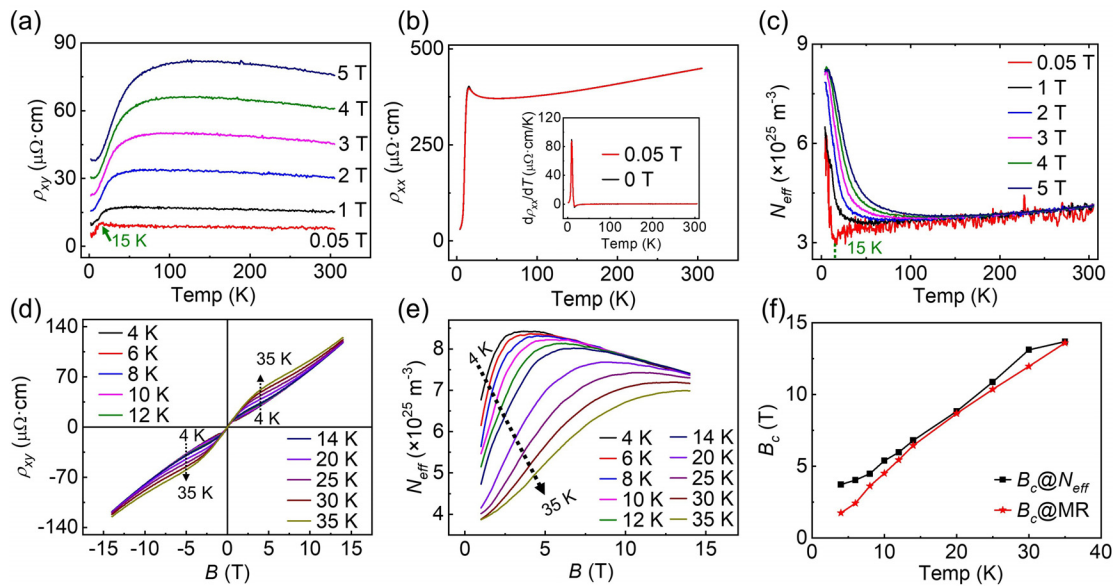


FIG. 2. (a) $\rho_{xy} \sim T$ curves from 300 to 4 K under different external fields. The data measured at 0.05 T are displayed as ten times of the original data (red curve). (b) The $\rho_{xx} \sim T$ curves and $d\rho_{xx}/dT \sim T$ curves in the inset measured under 0.05 T (red line) and 0 T (black line). (c) The corresponding temperature-dependent N_{eff} under different external fields. (d) External field-dependent ρ_{xy} at different temperatures. (e) External field-dependent N_{eff} at different temperatures. (f) Temperature dependence of the critical external fields extracted from Fig. 1(a) ($B_c@MR$) and extracted from Fig. 2(e) ($B_c@N_{eff}$).

crystals are in the PM state. Then the observable band variation emerges at 15 K [Fig. 3(b-IV)], which is consistent with the critical temperature of the PM–FM phase transition and the $\rho_{xx} \sim T$ curve under 0 T. Notably, the spin-up and spin-down valence subbands split with the crossing over of the spin-up valence and conduction subbands near the Fermi level at 10 K (see Fig. S11 and Refs. 17 and 28 for the identification of spin-up and spin-down sub-bands). Meanwhile, the carrier pockets are well-constructed and expand monotonically with the further decrement of the temperature [Figs. 3(b-V)–3(b-VII)], see Fig. S12 for the temperature-dependent Fermi level variation). Upon returning to 30 K, the band structure reverts to its initial state exactly [Fig. 3(b-VIII)].

The corresponding energy distribution curves (EDCs) around the X point at different temperatures exhibit a noticeable shift to the deeper energy at 15 K [Fig. 3(c)]. Meanwhile, the momentum distribution curves (MDCs) at different temperatures show that the spin-up conduction subband starts to intersect the Fermi level, and a small carrier pocket emerges at 15 K [Fig. 3(d)], which elucidates the sudden upward of the temperature-dependent N_{eff} at 15 K under 0.05 T. Moreover, the bottom of the spin-up conduction subband [E_C , marked in Fig. 3(b-VI)] gradually descends with the temperature decreasing [Fig. S6(a)]. The splitting and crossing of the bands originate from the strong exchange coupling between the band electrons and the local 4f moments,^{17,30} which contribute to the magnetization of EuB₆ (referring to Note 3 of the supplementary material). The absolute value of E_C ($|E_C|$) is plotted as a function of M/M_{max} at different temperatures [Fig. 3(e)]. M/M_{max} is derived from the $M \sim T$ curve measured under

0.005 T, where M_{max} is the maximum measured magnetization of the curve and M is the measured magnetization of the curve at different temperatures [Figs. S6(b) and S6(c)]. It should be noted that, M/M_{max} can actually reflect the temperature-dependent magnetization ratio under the zero external field because the tiny field barely changes the intrinsic magnetic state in EuB₆ (see Fig. S4 for a detailed analysis). $|E_C|$ is positively correlated with M/M_{max} which indicates that the enhanced temperature-dependent magnetization ratio in EuB₆ plays a crucial role in promoting the topological phase transition. Considering the strong exchange coupling between the band electrons and the local 4f moments, it can be further inferred that the larger field-induced magnetization should also promote the topological phase transition of EuB₆ (Ref. 31) (for a detailed analysis, see Note 3 of the supplementary material), which is called as the field-induced topological phase transition.^{11,16,32} Moreover, $|E_C|$ is positively correlated with N_{eff} measured at different temperatures [Fig. 3(f)], which implies that the larger N_{eff} means the larger $|E_C|$ of the electron band. Note that, N_{eff} in Fig. 3(f) is derived from the $\rho_{xy} \sim T$ curve measured under 0.05 T, which can actually reflect the N_{eff} under 0 T, as proved in Fig. 2(b).

To elucidate the field-induced topological phase transition, the field-induced band variation should be confirmed. Since ARPES measurements cannot be carried out under the external fields, KPFM^{33,34} is employed to investigate the field-dependent relative chemical potential (CP) of EuB₆, reflecting the Fermi level (E_F) variation. In the experiment, the patterned nonmagnetic Ti/Au(5/50 nm) thin films are sequentially deposited on the EuB₆ surface to serve as the buffer and the reference layer (see details in Fig. S7). As shown in Fig. 4(a), the

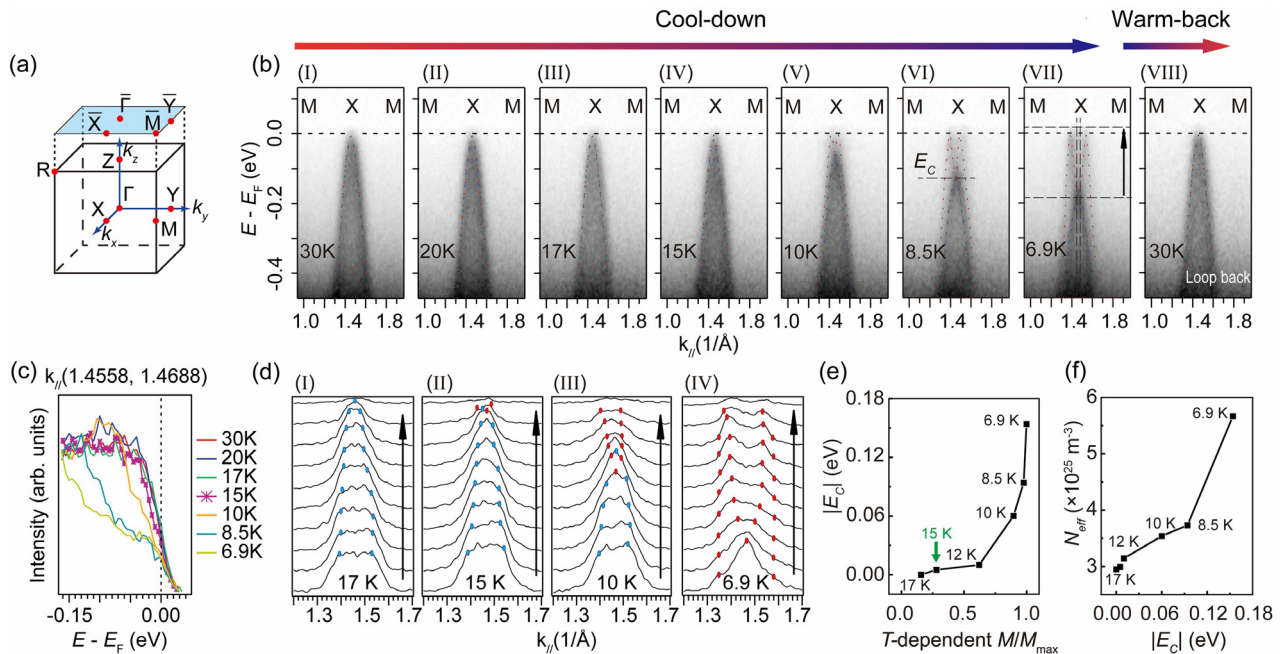


FIG. 3. (a) Bulk and (001)-surface Brillouin zones of EuB₆. (b) Intensity plots of the ARPES data along M-X, displaying the corresponding band structures at different temperatures. The red and blue thin dashed lines marked the spin-up and spin-down subbands. E_C denotes the energy of the bottom of the spin-up conduction band, with respect to the Fermi level. (c) Energy distribution curves (EDCs) around the X point at different temperatures, with $k_{||}$ ranging from 1.4558 to 1.4688 Å⁻¹, as indicated by the vertical dashed lines in Fig. 3(b-VII). (d) Momentum distribution curves (MDCs) below the Fermi level, within the range indicated by the horizontal dashed lines in Fig. 3(b-VII). (e) $|E_C|$ as a function of M/M_{max} at different temperatures. (f) The relationship between $|E_C|$ and the corresponding N_{eff} at different temperatures.

yellow and black areas in the typical CP mapping encompassing both the Au film and the EuB₆ surfaces reflect the intrinsic difference of the CP between EuB₆ and the Au film, which can be further associated with the corresponding difference of E_F . The position-dependent CP curves along the line-cut under different external fields are presented in Fig. 4(b). Referring to the bottom flat parts (the CP of the Au film) of the curves as 0 V, the top-left flat parts of the curves (the relative CP of EuB₆) shift downward under large external fields. The shift can be quantitatively expressed as $\Delta CP = CP(B) - CP(0)$, where $CP(0)$ and $CP(B)$ denote the relative CP of EuB₆ under the zero and finite external fields. ΔCP relates to the field-induced variation of the Fermi level ($\Delta E_F = e \Delta CP$). As shown in Fig. 4(c), the noticeable field-dependent downshift of the CP is observed at different temperatures, and the magnitude of ΔCP becomes larger at higher temperatures (see detailed data in Fig. S8), especially ΔCP is more than -10 mV from 10 to 20 K, where the CNMR ratio exceeding -80% appears. The above-mentioned results indicate a strong correlation between the field-induced band variation and CNMR and suggest that the band structures near the Fermi level are substantially altered by the external field.

To investigate the influence of the field-induced band variation on N_{eff} , the relationships between N_{eff} and the field-induced magnetization ratio $[M/M_s]$, where M is the field-induced magnetization, and M_s is the saturation magnetization of EuB₆ at 4 K, referring to Fig. S4 (a)] at different temperatures are constructed in Fig. 4(d). Since the monotonic increase in N_{eff} with the temperature-dependent magnetization ratio (Fig. S9) originates from the temperature-induced

topological phase transition, it can be concluded that the monotonic increase in N_{eff} with the field-induced magnetization ratio [Fig. 4(d)] originates from the field-induced topological phase transition. With a higher field-induced magnetization ratio, the degree of the band splitting and crossing over near the Fermi level becomes larger, which consequently leads to the larger carrier pockets near the Fermi level and a larger value of N_{eff} . Since no distinct electronic conductivity domain in the EuB₆ single crystal was observed in our KPFM measurement [Fig. S7(c)], it indicates the absence of the electronic phase separation. In addition, the negative MR ratio contributed by the Kondo-like upwarp is $\sim -8\%$. The negative MR ratio arising from the scattering effect between electrons and magnetic domain walls in a homogeneous magnetic system is usually $\sim -2\%$ or smaller.^{35,36} Those negative MR ratios are much smaller than the observed CNMR $\sim -88\%$ in EuB₆. Combined with the $\rho_{xx} \sim T$ curve under 0 T [Fig. 1(c)] and the ARPES results [Fig. 3(b)], the resistivity dropped more than 90% when the band splitting and crossing happened from 15 to 4 K, which demonstrates that the band splitting and crossing can result in a resistivity drop of more than 90%. Since the field-induced band splitting and crossing named as the field-induced topological phase transition has been proved and other possible mechanisms cannot afford such a huge CNMR ratio, it can be concluded that the CNMR in EuB₆ predominantly arises from the magnetic field-induced topological phase transition.

In conclusion, the transport properties and the band structure variations of EuB₆ have been systematically investigated, revealing the

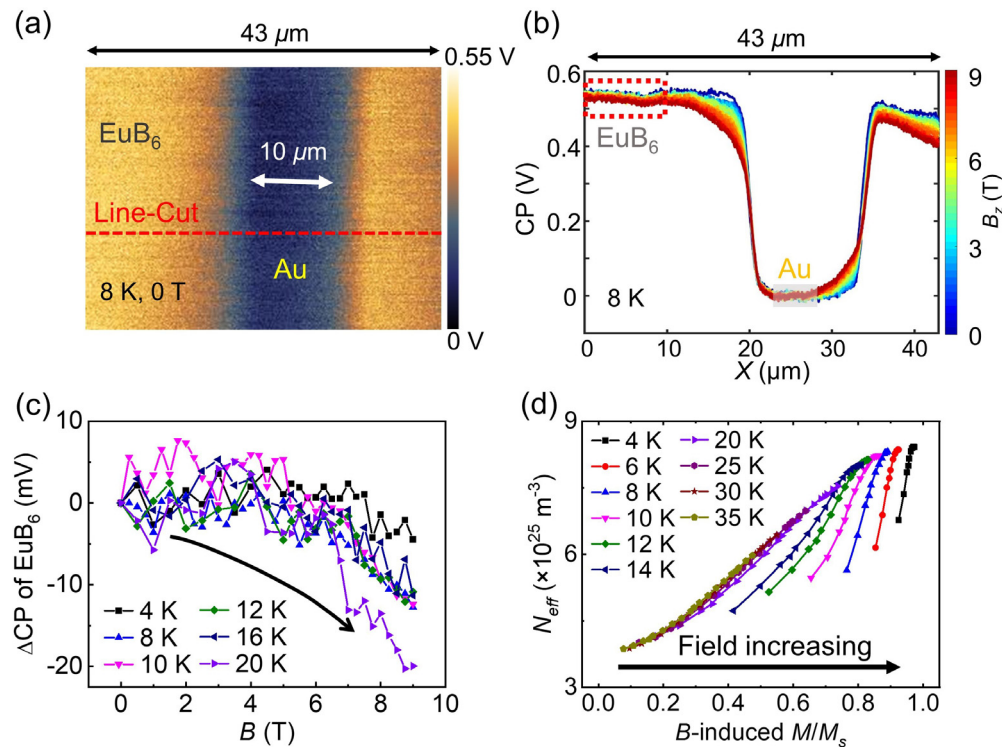


FIG. 4. (a) The relative CP mapping on the designed EuB₆ sample surface, encompassing both the deposited Au film surface (black) and the EuB₆ surface (yellow). (b) The relative CP under different external fields (0–9 T) measured along the line-cut in (a). (c) The relative CP variation (ΔCP) of EuB₆ as a function of the external field at different temperatures. (d) The relationship between N_{eff} and the field-induced magnetization ratio M/M_s at different temperatures.

magnetic field-induced topological phase transition as the primary mechanism for the CNMR. The ARPES results show the gradual band splitting and crossing near the Fermi level below 15 K, and further deduce that the band structure variation is responsible for the monotonic increment relationship between the effective carrier concentration and the temperature-dependent magnetization ratio. In addition, the band splitting and crossing over near the Fermi level should be promoted by the external magnetic field, which is supported by both the field-induced variation of the Fermi level based on the KPFM results and the monotonic increment relationship between the effective carrier concentration and the field-induced magnetization ratio. Furthermore, by excluding other mechanisms, it is finally concluded that the CNMR in EuB_6 predominantly arises from the magnetic field-induced topological phase transition originating from the strong exchange coupling between the band electrons and the local $4f$ moments. This work proposes a reasonable mechanism for the CNMR, which is applicable to the magnetic topological materials. Furthermore, these findings provide a route for exploring and manipulating the topology-related transport properties of other systems with strong correlation between band electrons and magnetic moments via the external magnetic field.

See the [supplementary material](#) for the sample preparation, structure characterization, and more details of experiments and analysis.

This work was supported by the Ministry of Science and Technology of China (Nos. 2022YFA1204100 and 2023YFA1406301), the National Natural Science Foundation of China (Nos. 62488201 and 12274085), the Chinese Academy of Sciences (Nos. XDB33030000 and YSBR-053), the Innovation Program of Quantum Science and Technology (No. 2021ZD0302700), and the China Postdoctoral Science Foundation (No. 2024T170990).

AUTHOR DECLARATIONS

Conflict of Interest

The authors have no conflicts to disclose.

Author Contributions

Lulu Pan and Yunhao Wang contributed equally to this work.

Lulu Pan: Conceptualization (equal); Data curation (lead); Formal analysis (equal); Investigation (equal); Methodology (equal); Validation (equal); Visualization (equal); Writing – original draft (equal); Writing – review & editing (equal). **Yunhao Wang:** Conceptualization (equal); Formal analysis (equal); Investigation (equal); Validation (equal); Visualization (equal); Writing – original draft (supporting); Writing – review & editing (supporting). **Xiang Ding:** Formal analysis (equal); Investigation (equal); Visualization (equal); Writing – original draft (supporting); Writing – review & editing (supporting). **Guojing Hu:** Formal analysis (supporting); Funding acquisition (supporting); Investigation (equal); Writing – original draft (equal); Writing – review & editing (equal). **Hui Guo:** Formal analysis (equal); Funding acquisition (supporting); Investigation (equal); Writing – original draft (equal); Writing – review & editing (equal). **Senhao Lv:** Formal analysis (supporting); Investigation (equal); Validation (equal); Writing – original draft (supporting); Writing –

review & editing (supporting). **Guoyu Xian:** Formal analysis (supporting); Investigation (equal); Validation (supporting); Writing – review & editing (supporting). **Qi Qi:** Formal analysis (supporting); Investigation (supporting); Writing – review & editing (supporting). **Ke Zhu:** Investigation (supporting); Validation (supporting); Writing – review & editing (supporting). **Ye chao Han:** Formal analysis (supporting); Investigation (supporting); Writing – review & editing (supporting). **Minyinan Lei:** Investigation (supporting); Validation (supporting); Writing – review & editing (supporting). **Zhuolin Li:** Investigation (supporting). **Lihong Bao:** Funding acquisition (supporting); Resources (supporting). **Ying Zhang:** Resources (supporting). **Xiao Lin:** Resources (supporting). **Shiyu Zhu:** Formal analysis (equal); Investigation (supporting); Resources (equal); Visualization (supporting); Writing – original draft (equal); Writing – review & editing (equal). **Rui Peng:** Formal analysis (equal); Funding acquisition (supporting); Investigation (supporting); Resources (equal); Visualization (equal); Writing – original draft (supporting); Writing – review & editing (supporting). **Hai-Tao Yang:** Conceptualization (equal); Formal analysis (equal); Funding acquisition (equal); Project administration (lead); Resources (equal); Supervision (equal); Visualization (equal); Writing – original draft (equal); Writing – review & editing (equal). **Hong-Jun Gao:** Funding acquisition (equal); Project administration (supporting); Supervision (lead).

DATA AVAILABILITY

The data that support the findings of this study are available from the corresponding authors upon reasonable request.

REFERENCES

- B. J. Wieder, B. Bradlyn, J. Cano, Z. J. Wang, M. G. Vergniori, L. Elcoro, A. A. Soluyanov, C. Felser, T. Neupert, N. Regnault, and B. A. Bernevig, *Nat. Rev. Mater.* **7**, 196–216 (2021).
- Q. L. He, T. L. Hughes, N. P. Armitage, Y. Tokura, and K. L. Wang, *Nat. Mater.* **21**, 15–23 (2022).
- M. J. Gilbert, *Commun. Phys.* **4**, 70 (2021).
- K. v. Klitzing, G. Dorda, and M. Pepper, *Phys. Rev. Lett.* **45**, 494–497 (1980).
- K. v. Klitzing, *Annu. Rev. Condens. Matter Phys.* **8**, 13–30 (2017).
- R. Yu, W. Zhang, H.-J. Zhang, S.-C. Zhang, X. Dai, and Z. Fang, *Science* **329**, 61–64 (2010).
- C.-Z. Chang, J. Zhang, X. Feng, J. Shen, Z. Zhang, M. Guo, K. Li, Y. Ou, P. Wei, L.-L. Wang, Z.-Q. Ji, Y. Feng, S. Ji, X. Chen, J. Jia, X. Dai, Z. Fang, S.-C. Zhang, K. He, Y. Wang, L. Lu, X.-C. Ma, and Q.-K. Xue, *Science* **340**, 167–170 (2013).
- B. A. Bernevig, C. Felser, and H. Beidenkopf, *Nature* **603**, 41–51 (2022).
- E. Liu, Y. Sun, N. Kumar, L. Muechler, A. Sun, L. Jiao, S.-Y. Yang, D. Liu, A. Liang, Q. Xu, J. Kroder, V. Süß, H. Borrmann, C. Shekhar, Z. Wang, C. Xi, W. Wang, W. Schnelle, S. Wirth, Y. Chen, S. T. B. Goennenwein, and C. Felser, *Nat. Phys.* **14**, 1125–1132 (2018).
- Y. Deng, Y. Yu, M. Z. Shi, Z. Guo, Z. Xu, J. Wang, X. H. Chen, and Y. Zhang, *Science* **367**, 895–900 (2020).
- G. Zheng, X. Zhu, Y. Liu, J. Lu, W. Ning, H. Zhang, W. Gao, Y. Han, J. Yang, H. Du, K. Yang, Y. Zhang, and M. Tian, *Phys. Rev. B* **96**, 121401(R) (2017).
- A. Gaikwad, S. Sun, P. Wang, L. Zhang, J. Cano, X. Dai, and X. Du, *Commun. Mater.* **3**, 94 (2022).
- R. Tang, F. Boi, and Y. H. Cheng, *npj Quantum Mater.* **8**, 78 (2023).
- J. Y. You, X. J. Dong, B. Gu, and G. Su, *Phys. Rev. B* **103**, 104403 (2021).
- J. L. Collins, A. Tadich, W. Wu, L. C. Gomes, J. N. B. Rodrigues, C. Liu, J. Hellerstedt, H. Ryu, S. Tang, S. K. Mo, S. Adam, S. A. Yang, M. S. Fuhrer, and M. T. Edmonds, *Nature* **564**, 390–394 (2018).
- Y. Satake, J. Shiozai, G. P. Mazur, S. Kimura, S. Awaji, K. Fujiwara, T. Nojima, K. Nomura, S. Souma, T. Sato, T. Dietl, and A. Tsukazaki, *Phys. Rev. Mater.* **4**, 044202 (2020).

- ¹⁷S. Nie, Y. Sun, F. B. Prinz, Z. Wang, H. Weng, Z. Fang, and X. Dai, *Phys. Rev. Lett.* **124**, 076403 (2020).
- ¹⁸S. Süllo, I. Prasad, S. Bogdanovich, M. C. Aronson, J. L. Sarrao, and Z. Fisk, *J. Appl. Phys.* **87**, 5591–5593 (2000).
- ¹⁹X. Zhang, L. Yu, S. von Molnar, Z. Fisk, and P. Xiong, *Phys. Rev. Lett.* **103**, 106602 (2009).
- ²⁰J. Yuan, X. Shi, H. Su, X. Zhang, X. Wang, N. Yu, Z. Q. Zou, W. W. Zhao, J. P. Liu, and Y. F. Guo, *Phys. Rev. B* **106**, 054411 (2022).
- ²¹S. Y. Gao, S. Xu, H. Li, C. J. Yi, S. M. Nie, Z. C. Rao, H. Wang, Q. X. Hu, X. Z. Chen, W. H. Fan, J. R. Huang, Y. B. Huang, N. Pryds, M. Shi, Z. J. Wang, Y. G. Shi, T. L. Xia, T. Qian, and H. Ding, *Phys. Rev. X* **11**, 021016 (2021).
- ²²Z. Fisk, D. C. Johnston, B. Cornut, S. V. Molnar, S. Oseroff, and R. Calvo, *J. Appl. Phys.* **50**, 1911–1913 (1979).
- ²³G. Long, S. Xu, X. Cai, Z. Wu, T. Han, J. Lin, C. Cheng, Y. Cai, X. Wang, and N. Wang, *Nanotechnology* **29**, 035204 (2018).
- ²⁴H. Liu, Y. Xue, J.-A. Shi, R. A. Guzman, P. Zhang, Z. Zhou, Y. He, C. Bian, L. Wu, R. Ma, J. Chen, J. Yan, H. Yang, C. M. Shen, W. Zhou, L. Bao, and H. J. Gao, *Nano Lett.* **19**, 8572–8580 (2019).
- ²⁵G.-M. Zhang, Y.-F. Yang, and F.-C. Zhang, *Phys. Rev. B* **101**, 020501(R) (2020).
- ²⁶S. Süllo, I. Prasad, M. C. Aronson, J. L. Sarrao, Z. Fisk, D. Hristova, A. H. Lacerda, M. F. Hundley, A. Vigliante, and D. Gibbs, *Phys. Rev. B* **57**, 5860–5869 (1998).
- ²⁷B. Kang, Z. Liu, D. Zhao, L. Zheng, Z. Sun, J. Li, Z. Wang, T. Wu, and X. Chen, *Adv. Mater.* **34**, 2201597 (2022).
- ²⁸W. L. Liu, X. Zhang, S. M. Nie, Z. T. Liu, X. Y. Sun, H. Y. Wang, J. Y. Ding, Q. Jiang, L. Sun, F. H. Xue, Z. Huang, H. Su, Y. C. Yang, Z. C. Jiang, X. L. Lu, J. Yuan, S. Cho, J. S. Liu, Z. H. Liu, M. Ye, S. L. Zhang, H. M. Weng, Z. Liu, Y. F. Guo, Z. J. Wang, and D. W. Shen, *Phys. Rev. Lett.* **129**, 166402 (2022).
- ²⁹C.-H. Min, B. Kang, B. K. Cho, E.-J. Cho, B.-G. Park, and H.-D. Kim, *J. Korean Phys. Soc.* **79**, 734–740 (2021).
- ³⁰J. Kunes and W. E. Pickett, *Phys. Rev. B* **69**, 165111 (2004).
- ³¹J. Kim, W. Ku, C.-C. Lee, D. S. Ellis, B. K. Cho, A. H. Said, Y. Shvyd'ko, and Y.-J. Kim, *Phys. Rev. B* **87**, 155104 (2013).
- ³²K. Ueda, T. Oh, B.-J. Yang, R. Kaneko, J. Fujioka, N. Nagaosa, and Y. Tokura, *Nat. Commun.* **8**, 15515 (2017).
- ³³F. Wu, Q. Li, P. Wang, H. Xia, Z. Wang, Y. Wang, M. Luo, L. Chen, F. Chen, J. Miao, X. Chen, W. Lu, C. Shan, A. Pan, X. Wu, W. Ren, D. Jariwala, and W. Hu, *Nat. Commun.* **10**, 4663 (2019).
- ³⁴Y. Vaknin, R. Dagan, and Y. Rosenwaks, *Nanomaterials* **10**, 2346 (2020).
- ³⁵J. F. Gregg, W. Allen, K. Ounadjela, M. Viret, M. Hehn, S. M. Thompson, and J. M. D. Coey, *Phys. Rev. Lett.* **77**, 1580–1583 (1996).
- ³⁶U. Rüdiger, J. Yu, L. Thomas, S. S. P. Parkin, and A. D. Kent, *Phys. Rev. B* **59**, 11914–11918 (1999).